

The Impact of Cloud Radiative Feedback, Remote ENSO Forcing, and Entrainment on the Persistence of North Pacific Sea Surface Temperature Anomalies

SUNGSU PARK

Advanced Study Program, National Center for Atmospheric Research, Boulder, Colorado

MICHAEL A. ALEXANDER

NOAA/Earth System Research Laboratory, Boulder, Colorado

CLARA DESER

Climate and Global Dynamics Division, National Center for Atmospheric Research, Boulder, Colorado

(Manuscript received 16 March 2005, in final form 24 January 2006)

ABSTRACT

The influence of cloud radiative feedback, remote ENSO heat flux forcing, and oceanic entrainment on persisting North Pacific sea surface temperature (SST) anomalies is investigated using a stochastically forced ocean mixed layer model. The stochastic heat flux is estimated from an atmospheric general circulation model, the seasonally varying radiative feedback parameter and remote ENSO forcing are obtained from observations, and entrainment is derived from the observed mean seasonal cycle of ocean mixed layer depth. Persistence is examined via SST autocorrelations in the western, central, and subtropical eastern North Pacific and for the leading pattern of variability across the basin. The contribution of clouds, ENSO, and entrainment to SST persistence is evaluated by comparing simulations with and without each term.

The SST autocorrelation structure in the model closely resembles nature: the pattern correlation between the two is 0.87–0.9 in the three regions and for the basinwide analyses, and 0.35–0.66 after subtracting an exponential function representing the background damping resulting from air–sea heat fluxes. Positive radiative feedback enhances SST autocorrelations (~ 0.1 – 0.3) from late spring to summer in the central and western Pacific and from late summer to fall in the subtropical eastern Pacific. The influence of the remote ENSO forcing on SST autocorrelation varies with season and location with a maximum impact on the correlation magnitude of 0.2–0.3. The winter-to-winter recurrence of higher autocorrelations is caused by entrainment, which generally suppresses SST variability but returns thermal anomalies sequestered beneath the mixed layer in summer back to the surface in the following fall/winter. This reemergence mechanism enhances SST autocorrelation by ~ 0.3 at lags of 9–12 months from the previous winter in the western and central Pacific, but only slightly enhances autocorrelation (~ 0.1) in the subtropical eastern Pacific.

The impact of clouds, ENSO, and entrainment on the autocorrelation structure of the basinwide SST anomaly pattern is similar to that in the western region. ENSO's impact on the basinwide North Pacific SST autocorrelation in an atmospheric general circulation model coupled to an ocean mixed layer model with observed SSTs specified in the tropical Pacific is very similar to the results from the stochastic model developed here.

1. Introduction

Extratropical air–sea interactions have the potential to influence many aspects of the climate system. For

example, sea surface temperature (SST) anomalies in the North Pacific are closely associated with summer precipitation and drought over North America (Barlow et al. 2001). In turn, the summer subtropical high over the North Pacific, which is strongly influenced by diabatic heating over the continental United States (Hoskins 1996), may feed back on preexisting SST anomalies by modulating marine stratiform clouds and downwelling radiative fluxes at the sea surface (Klein et al.

Corresponding author address: Sungsu Park, Department of Atmospheric Sciences, University of Washington, ATG Building, Box 351640, Seattle, WA 98195-1640.
E-mail: sungsu@atmos.washington.edu

1995; Norris et al. 1998, Park et al. 2005). A greater knowledge of the factors that govern the evolution of extratropical SST anomalies may enhance our understanding and ability to predict important climate, ecosystem, and socioeconomic variability.

To first order, the persistence or decay time of mid-latitude SST anomalies can be simulated by a motionless, constant-depth mixed layer ocean model that is forced by rapidly varying (stochastic) atmospheric forcing and linearly damped by heat fluxes back to the atmosphere (Frankignoul and Hasselmann 1977). In this most basic stochastic model, the damping parameter is constant over the seasonal cycle and can be estimated by fitting an exponential function to the lagged autocorrelation of monthly SST anomalies. Several studies (e.g., Reynolds 1978; Frankignoul and Reynolds 1983; Frankignoul 1985; Herterich and Hasselmann 1987; Ostrovskii and Piterbarg 1995, 2000) extended the local stochastic forcing model to include advection, horizontal diffusion, and turbulent entrainment of water into the mixed layer. SST persistence is further influenced by the seasonal cycle of the mixed layer depth (MLD) through its impact on the ocean's thermal inertia and on the rate and the temperature of the water entrained into the mixed layer from below (Namias et al. 1988; Alexander and Penland 1996; Deser et al. 2003). However, the influence of several processes on North Pacific SST persistence over the course of the annual cycle have yet to be fully explored, including SST-radiation feedback, ENSO-induced surface flux anomalies, and the turbulent entrainment of temperature anomalies into the mixed layer.

Over the North Pacific, the fraction of marine stratiform clouds (MSCs) is greatest during summer (Klein and Hartmann 1993). MSC and SST variations are strongly coupled on monthly, interannual, and interdecadal time scales (Weare 1994; Norris and Leovy 1994; Norris 2000; Park and Leovy 2004). MSCs cool the ocean mixed layer in summer by reflecting incoming solar radiation. In turn, cold SSTs enhance the formation of MSCs by increasing the static stability, which traps moisture in the boundary layer and lowers the cloud base, thereby increasing the thermal and moisture coupling between the surface and the cloud layer (Bretherton and Wyant 1997; Park et al. 2004). This positive "SST-MSC" or "radiative" feedback has been hypothesized to be important for summer-to-winter and interannual persistence of North Pacific SST anomalies (Zhang et al. 1998; Norris et al. 1998). Recently, Park et al. (2005) found that positive radiative feedback can substantially enhance the persistence of SST anomalies in portions of the North Pacific in early summer.

ENSO strongly affects the atmospheric circulation and air-sea heat exchanges over the North Pacific Ocean during winter, when conditions are favorable for poleward planetary wave propagation from the tropical Pacific (Wallace and Gutzler 1981; Trenberth et al. 1998; Cayan 1992). These ENSO teleconnections drive changes in ocean basins remote from the equatorial Pacific; thus the atmosphere can act like a "bridge" between the tropical and North Pacific Ocean (e.g., Alexander 1992; Lau and Nath 1996; Alexander et al. 2002; Park 2004). Alexander et al. (2004) and Park and Leovy (2004) also found remote ENSO teleconnections over the western North Pacific during summer with meridional shifts of the jet stream, extratropical storm track and low-level cloud decks, and large-amplitude SST anomalies in the Kuroshio extension region. Because the persistence of ENSO varies with the seasons (Torrence and Webster 1998), ENSO is likely to have a complex influence on the persistence of North Pacific SSTs.

The mixed layer depth in the North Pacific Ocean undergoes a large seasonal cycle. During fall and winter, strong winds and surface cooling increase the MLD via the turbulent entrainment of water into the mixed layer from below. As a result the MLD reaches a maximum depth of ~100 (250) m in the eastern (western) North Pacific by February-March. The mixed layer reforms close to the surface in the following spring resulting from increased insolation and decreased wind mixing, resulting in minimum MLDs of ~10-30 m in July-August. Some of the thermal anomalies created in the deep winter mixed layer are sequestered in the statically stable seasonal thermocline (25-100 m) in summer, while air-sea fluxes strongly damp the concurrent SST anomalies. The subsurface anomalies are then reentrained into the surface layer during the following fall and winter when the ocean mixed layer deepens again. As a result, winter and spring SST anomalies recur in the following fall and winter, without persisting through the intervening summer. This process, first observed by Namias and Born (1970, 1974) and termed the "reemergence mechanism" by Alexander and Deser (1995), occurs over much of the North Pacific Ocean (Alexander et al. 1999), but its timing and strength depends on the month the anomaly was created and the annual cycle of MLD at that location.

The goal of our study is to understand how cloud radiative feedback, remote ENSO forcing, and oceanic entrainment contribute to the persistence of monthly SST anomalies in the North Pacific Ocean. To this end, we employ a stochastically forced entraining ocean mixed layer model used by Deser et al. (2003), but with

a more realistic representation of the stochastic forcing and atmospheric feedback parameters, and the addition of remote ENSO heat flux and Ekman forcing. The impact of each process on the SST persistence is assessed by comparing autocorrelations of monthly SST anomalies as a function of calendar month and lag in the full model to simulations in which one of the processes is excluded. In addition, results from the stochastic model are compared to those from an atmospheric general circulation model (AGCM) that has observed SSTs specified in the tropical Pacific and is coupled to a mixed layer model (MLM) over the remainder of the global oceans.

The paper is structured as follows. Section 2 provides a detailed description of the model and the methods used for estimating the model parameter values and forcing fields. We apply the stochastic model to the central western Pacific region in section 3, and to the central and subtropical eastern Pacific regions in section 4. The persistence of the dominant pattern of

North Pacific SST anomalies from the stochastic model and from the AGCM–MLM simulations, are examined in section 5. The results are summarized and discussed in section 6.

2. The stochastic ocean mixed layer model with remote ENSO forcing

A stochastically driven ocean mixed layer model, first introduced by Frankignoul and Hasselmann (1977), simulates the basic statistical properties of mid-latitude SST anomalies reasonably well (e.g., Frankignoul 1985). Following Deser et al. (2003), the stochastic model used here also contains a simplified entrainment term estimated from the seasonally varying climatological MLD in order to include the reemergence mechanism. We further added radiative feedback and remote ENSO heat flux and Ekman forcing terms, resulting in the following heat budget equation for the ocean mixed layer:

$$\rho C_p[\text{MLD}] \left(\frac{d}{dt} T' \right) = F' - (\lambda_{\text{LHF}+\text{SHF}} + \lambda_{\text{SW}+\text{LW}} + \lambda_{\text{res}}) T' + \rho C_p [W_e] (T'_b - T') + f'_{\text{ENSO}}, \quad (1)$$

where t is time, $[\]$ is the seasonally varying climatological mean, prime is an anomaly from the mean, T is the SST, F is the stochastic atmospheric heat flux and Ekman transport forcing, λ is the feedback parameter for each surface heat flux component [latent heat flux (LHF), sensible heat (SHF), shortwave (SW), and longwave (LW)], W_e is the entrainment rate, T_b is the temperature of sub-mixed layer water, f_{ENSO} is the remote ENSO heat flux and Ekman forcing, ρ is the density of seawater ($=1025 \text{ kg m}^{-3}$), and C_p is the specific heat of seawater at constant pressure ($=4000 \text{ J kg}^{-1} \text{ K}^{-1}$). We incorporated a residual feedback parameter λ_{res} to approximate the contribution of other oceanic feedbacks and to compensate for the errors in the model parameter and forcing values. One of the main simplifying assumptions in Eq. (1) is that the MLD follows a seasonally varying climatological mean, which neglects several additional ways by which entrainment can impact SSTs (e.g., Frankignoul 1985; Alexander et al. 2000). Temperature advection by anomalous Ekman currents is incorporated into the stochastic and ENSO forcing, but other advective components are not included.

A key aspect of our approach is that the heat flux feedback parameter and remote ENSO forcing are estimated directly from the observed monthly surface heat fluxes and SST anomalies as a function of season

and location. In the following sections, we will discuss how monthly values of the individual forcing and feedback terms are estimated on a 5° latitude \times 5° longitude grid. After interpolating the monthly values to daily values, the stochastic model was integrated with a daily time step for the nominal period of 1951–2002 (the years with reliable SST observations) using a third-order Adams–Bashforth method. The model's monthly SST anomalies on the 5° latitude \times 5° longitude grid were analyzed and compared with observations during 1953–2002, because the entrainment forcing is activated in the third year of the simulations.

While the remote ENSO forcing includes realistic long-term variations, the absence of dynamic ocean processes, such as subduction, Rossby waves, and geostrophic advection from the MLM, limits the model's ability to simulate low-frequency SST variations. Thus, we focus our analysis on interannual variations by subtracting the 10-yr running average from the monthly SST anomalies (equivalent to a high-pass filter with a half-power point at 12.5 yr).

a. Stochastic forcing

To estimate the atmospheric stochastic forcing, feedback of the ocean on the surface heat fluxes should first be removed. Because the observed surface heat fluxes always contain oceanic feedback, we estimate the sto-

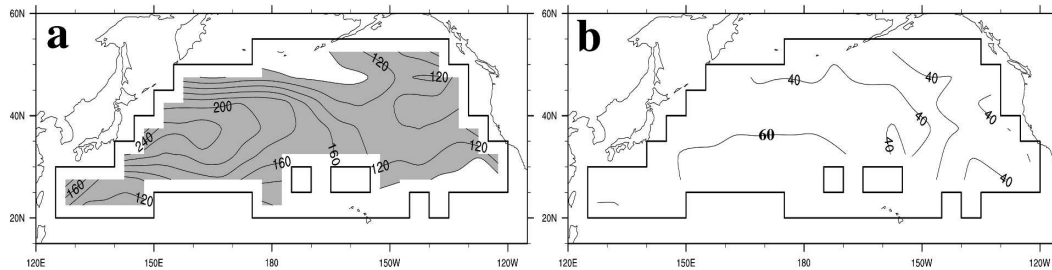


FIG. 1. The total standard deviation of the daily net surface heat flux (LHF + SHF + SW + LW) + Ekman transport anomalies during (a) January and (b) July obtained from 10 yr of a CAM3 control simulation. The contour interval is 20 W m^{-2} , and shading indicates values $>100 \text{ W m}^{-2}$.

chastic forcing from a simulation of the Community Atmospheric Model [(CAM3), the most recent version of the National Center for Atmospheric Research (NCAR) AGCM], which is forced by seasonally varying climatological SSTs. Using the last 10 yr of a 15-yr simulation, we calculated the total downward daily surface heat flux anomalies by summing the latent, sensible, shortwave, and longwave fluxes and the implicit Ekman heat transport, where the latter only includes fluctuations in the wind.

The standard deviation of the surface fluxes is shown for January and July in Figs. 1a,b, respectively. In January, the greatest flux variability occurs along a zonal band extending along $\sim 35^\circ\text{N}$, with values exceeding 200 W m^{-2} west of the date line. Relatively weak variability occurs over the northwestern and subtropical eastern Pacific Ocean. The flux variability is substantially weaker in summer than in winter, but it still exceeds 40 W m^{-2} over most of the basin.

The stochastic forcing fields are derived by first randomly selecting monthly values (with replacement), where the months follow the calendar but the year is randomly chosen from the last 10 yr of the CAM3 simulation. For example, a given reconstructed time series could be ordered as follows: January (year 5), February (year 2), March (year 5), . . . , December (year 8). This resampling is repeated to form a 52-yr time series. Then the consecutive daily fluxes over the North Pacific within each month of the time series is used to drive the stochastic ocean model. Because the decorrelation time scale of the surface fluxes is 1–3 days (not shown), this resampling procedure nearly preserves the persistence, spatial continuity, and magnitude of the original flux variability. Daily surface fluxes obtained from the National Centers for Environmental Prediction (NCEP)–NCAR reanalysis during 1951–2002 that have been high-pass filtered ($< \sim 30$ days) to partially remove air–sea feedback and remote forcing produced similar estimates of the stochastic forcing presented in Fig. 1 (not shown).

b. Heat flux feedback parameters

The heat flux feedback parameter (λ) values used in this study are from Park et al. (2005). They estimated λ from the observed monthly anomalies of SST and the surface heat fluxes over most of the world's oceans on a 5° latitude \times 10° longitude grid, which has been interpolated to $5^\circ \times 5^\circ$ grid for this study. Figure 2 shows the turbulent (SHF + LHF; upper), radiative (SW + LW; middle) and net (lower) heat flux feedback parameters during January (left) and July (right), where positive values indicate negative feedback on the SST anomalies. The turbulent heat flux feedback damps SST anomalies ($\lambda_{\text{SHF}+\text{LHF}} > 0$) for all seasons with maximum (minimum) damping during winter (summer) when the mean surface wind is strongest (weakest) and the moistening and warming of the near-surface air over warm SST anomalies is relatively weak (strong). Areas of strong damping are located over the far western subtropical Pacific Ocean and north of the Hawaii Islands during winter. During spring and summer the radiative feedback is generally positive ($\lambda_{\text{SW}+\text{LW}} < 0$) in the midlatitude North Pacific, with a magnitude comparable to that of $\lambda_{\text{SHF}+\text{LHF}}$. The positive radiative feedback over the central and eastern North Pacific Ocean is mainly due to strong SW feedback resulting from variations in the fraction of MSCs and fog. The net surface heat flux feedback is generally negative with the strongest (weakest) damping during winter (summer), but regions of weak, positive feedback occur over the northwestern and northeastern Pacific during summer. A more detailed discussion of the feedbacks is given in Park et al. (2005).

c. Remote ENSO forcing

The seasonally dependent remote ENSO forcing is estimated as follows. First, ENSO indices were obtained from EOF analysis of monthly SST anomalies over the tropical Pacific and Indian Oceans during 1951–2002. The first three modes, which are well sep-

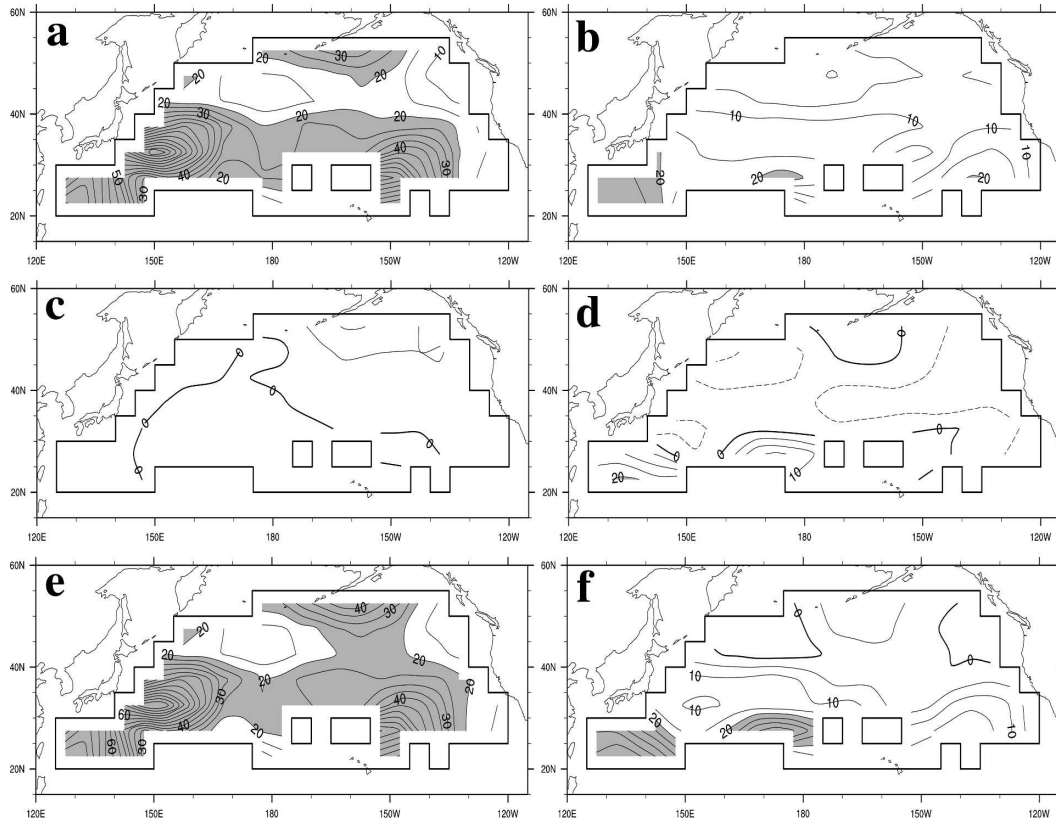


FIG. 2. The heat flux feedback parameters derived from observations (see Park et al. 2005). The (a), (b) turbulent (LHF + SHF), (c), (d) radiative, and (e), (f) net feedback values during January (left) and July (right). The contour interval is $5 \text{ W m}^{-2} \text{ K}^{-1}$ with solid (dashed) lines for positive (negative) values. Shading indicates values $> 20 \text{ W m}^{-2} \text{ K}^{-1}$.

rated from the others by the criteria of North et al. (1982) and have major centers of variance along the equator, were chosen to represent ENSO. The first principal component (PC)—the time series giving the amplitude and polarity of the leading EOF—primarily represents the variability associated with the mature phase of ENSO and is highly correlated with the Niño-3.4 index. The second PC exhibits an increasing trend with decadal variations, somewhat similar to the variability in Deser et al.'s (2004) tropical climate index, while the third PC is similar to the trans-Niño index (TNI; Trenberth and Stepaniak 2001; not shown). Then, the simultaneous seasonal regression anomalies of surface turbulent heat fluxes and Ekman heat transport on each standardized PCs were estimated using 42 yr (1956–97) of ship-observed monthly turbulent heat fluxes and 17 yr (1984–2000) of satellite-derived monthly radiative fluxes as described in Park et al. (2005). Although the PCs based on all months are orthogonal to each other, seasonal subsets of the PCs are not. Thus, to avoid counting the ENSO-induced forcings by different PCs multiple times, seasonal flux

anomalies for a specific ENSO mode were estimated by regressing the *residual* monthly heat flux anomalies, which do not contain any flux components that simultaneously vary with the other ENSO PCs. However, these regression anomalies include *local* feedback effects that are already parameterized in the stochastic model [Eq. (1)]. We estimated this local feedback by multiplying the simultaneous ENSO regression anomalies of SST by the net heat flux feedback (Fig. 2). The direct monthly ENSO forcing at each grid point was then calculated as follows:

$$f_{\text{ENSO}}^i(t) = \sum_{k=1}^3 [R_{k,\text{Ekman}} + \sum_{i=1}^4 (R_{k,i} + \lambda_i R_{k,T})] E_k(t), \quad (2)$$

where R is the regression of flux anomalies on ENSO, k and i are the indices of the ENSO modes and surface heat flux components, respectively, and E is the standardized ENSO PCs for the period of 1951–2002.

The downward surface heat flux and Ekman trans-

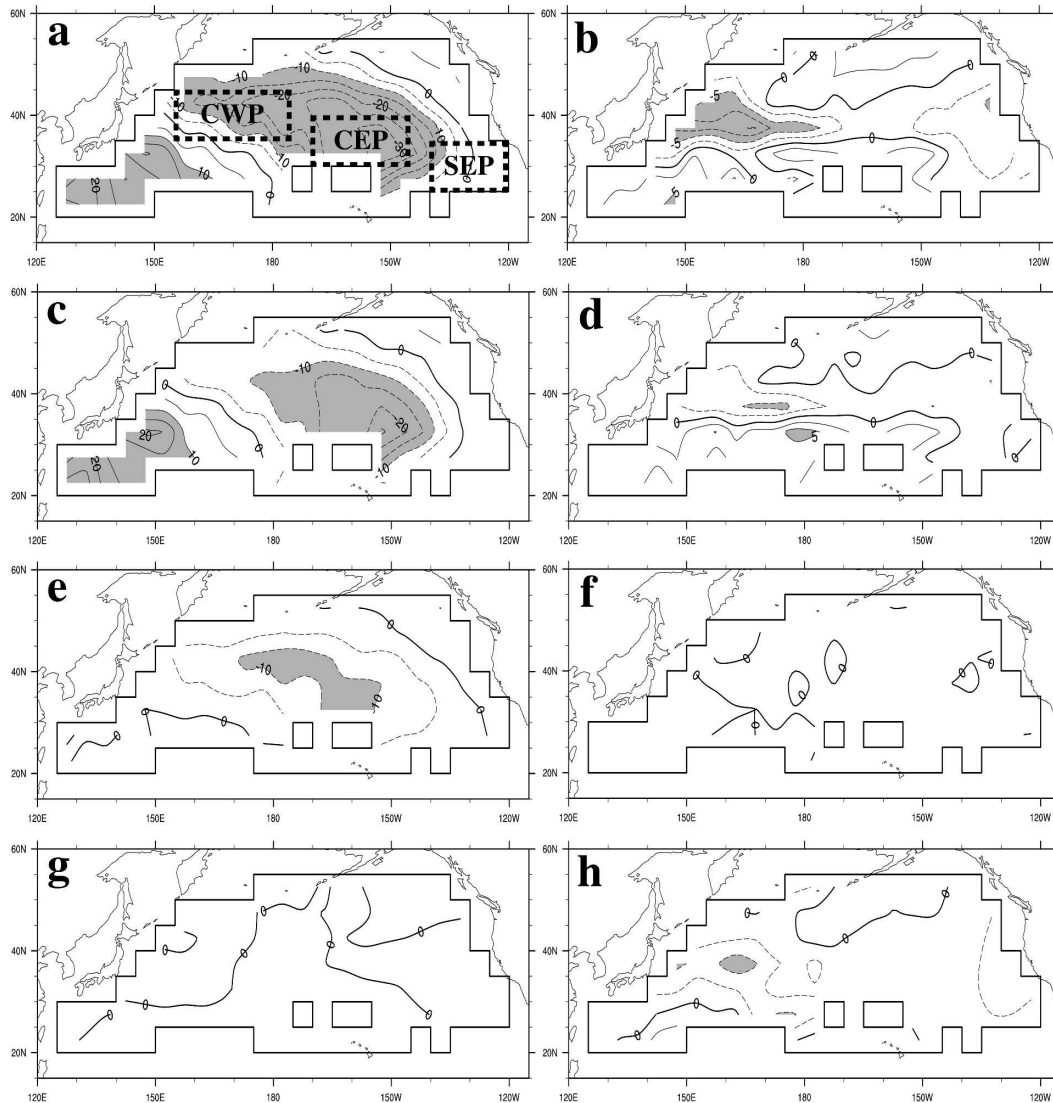


FIG. 3. Standardized ENSO regression anomalies, corrected for local air–sea feedback, of the (a), (b) total (net surface heat flux + Ekman), (c), (d) turbulent, (e), (f) Ekman, and (g), (h) radiative heat fluxes into the ocean during January (left; contour interval 5 W m^{-2} , with shading for values $>|10| \text{ W m}^{-2}$) and July (right; contour interval 2.5 W m^{-2} , with shading for values $>|5| \text{ W m}^{-2}$) regressed on the first PC of SST anomalies in the tropical Pacific–Indian Oceans. The three regions discussed in sections 3 and 4 are also indicated in (a).

port anomalies associated with the first ENSO mode, corrected for local feedback effect, are shown in Fig. 3. During January, the remote ENSO forcing strongly cools the central North Pacific with maximum amplitude over 30 W m^{-2} at 35°N , 152.5°W . About $2/3$ of this cooling is from the turbulent heat fluxes, with the remainder from Ekman transport. Positive anomalies occur in the southwestern and eastern parts of the domain, where the warming in the former exceeds 20 W m^{-2} and is largely due to the anomalous turbulent heat fluxes. During July, the ENSO-induced heat fluxes cool

the ocean along 37.5°N to the west of the date line with a maximum magnitude of $\sim 10 \text{ W m}^{-2}$ (Fig. 3b), consistent with Alexander et al. (2004) and Park and Leovy (2004). About half of this cooling is from SHF + LHF and the remaining half is from SW + LW, which is in contrast to January when the radiative contribution is negligible. Although weaker than in winter, the bridge-induced forcing still has a significant influence on the SST tendency during summer, because the mixed layer is very shallow (about 5%–15% of the MLD in winter) and thus has low thermal inertia.

d. Oceanic entrainment

In our study, the entrainment rate is defined by the tendency of the seasonally varying climatological MLD, that is, $[W_e] = d[\text{MLD}]/dt$ when the mixed layer deepens and $[W_e] = 0$ when it shoals. The MLD is obtained from Monterey and Levitus (1997) based on a potential density criterion. Unrealistic MLD values at a few points in the northwest Pacific were replaced using interpolation, and the MLD was constrained to be greater than 10 m to prevent the simulated SST anomalies from becoming unreasonably large.

In Deser et al. (2003), the temperature anomaly of sub-mixed layer water (T'_b) at a given depth within the seasonal thermocline was set to the SST anomaly when the MLD shoaled above that depth. Here, we also allow T'_b to evolve according to

$$T'_b(t) = T'(t - \Delta t)\exp(-k\Delta t), \quad (3)$$

where Δt is the time period that seawater is sequestered in the seasonal thermocline and k is the *effective* diffusivity, which roughly represents damping from several processes, including eddy mixing and subduction. Although k is likely to be a function of location, we roughly estimated k to have a constant value of 10^{-8} s^{-1} by analyzing Deser et al.'s (2003) autocorrelation maps of subsurface temperature anomalies at several locations in the North Pacific.

e. Residual feedback parameter

Even though Eq. (1) incorporates many important physical processes, the amplitude of the simulated SST anomalies may be unrealistic because of neglected terms (e.g., advection) or errors in the model parameters and forcings. The impact of all of the error sources is crudely incorporated into the model by specifying a residual feedback parameter λ_{res} . Because the goal of this study is to simulate the statistical properties of the observed monthly SST anomalies, we estimated λ_{res} such that the variance of monthly SST anomalies is similar to the observed variance at each grid point.

The residual feedback over the North Pacific is shown in Fig. 4. The magnitude of λ_{res} is generally less than $10 \text{ W m}^{-2} \text{ K}^{-1}$, except for parts of the western North Pacific south of 35°N and the eastern subtropical Pacific near 27.5°N , 135°W . Because λ_{res} is calculated as a time-independent constant, it forces the simulated year-round variance of monthly SST anomalies to be realistic, but not the seasonal variance. The simulated monthly SST variance, however, is fairly realistic, because the model–observation pattern correlations range from 0.72 (April) to 0.92 (September) and the percentage difference between the two ranges from 11.3% (February) to 19.5% (August).

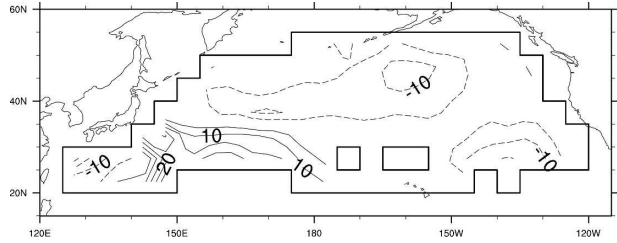


FIG. 4. The residual feedback parameter. Contour interval is $5 \text{ W m}^{-2} \text{ K}^{-1}$ with solid (dashed) lines for positive (negative) values.

3. The central western Pacific

In this section we explore the mechanisms responsible for the persistence of monthly SST anomalies in the central western Pacific region (CWP; $35^\circ\text{--}45^\circ\text{N}$, $155^\circ\text{E}\text{--}175^\circ\text{W}$; see Fig. 3a). This region was selected because it is characterized by homogeneous positive radiative feedback during summer (Fig. 2d), strong remote ENSO forcing both in January and July (Fig. 3), and a large annual cycle in MLD that is conducive for a strong reemergence signal (Deser et al. 2003). In addition, the maximum loading of the dominant pattern of North Pacific SST anomalies is located in the CWP region (Fig. 11a).

The annual cycle of the feedback parameters (larger positive values indicate greater damping) and MLD values in the CWP region are shown in Fig. 5a, while the magnitudes of stochastic and ENSO heat flux forcings are presented in Fig. 5b. The MLD is deepest during March (190 m) and shallowest during August (11 m), while the maximum and minimum damping occurs in November ($26 \text{ W m}^{-2} \text{ K}^{-1}$) and June ($-1 \text{ W m}^{-2} \text{ K}^{-1}$). Positive radiative feedback (as indicated by $\lambda_{\text{net}} < \lambda_{\text{LHF}} + \lambda_{\text{SHF}}$ in Fig. 5a) amplifies SST anomalies throughout the year, with the greatest effect during late spring–early summer. The stochastic forcing amplitude is largest during winter ($\sim 200 \text{ W m}^{-2}$) and smallest during summer ($\sim 50 \text{ W m}^{-2}$). Surface fluxes associated with the ENSO modes strongly force the ocean in the CWP region during January–March and August–September. We note that the ENSO-related heat flux forcing in this region is primarily associated with the first mode, except during summer when the magnitudes of the first two modes are comparable (not shown).

Although the magnitude of the ENSO-related forcing is much smaller than the stochastic forcing, the former should still have a strong influence on the SST persistence because the remote forcing is scaled by the standard deviation of the ENSO PC values, which can exceed 3, and more importantly, the ENSO forcing has much greater persistence than the stochastic forcing.

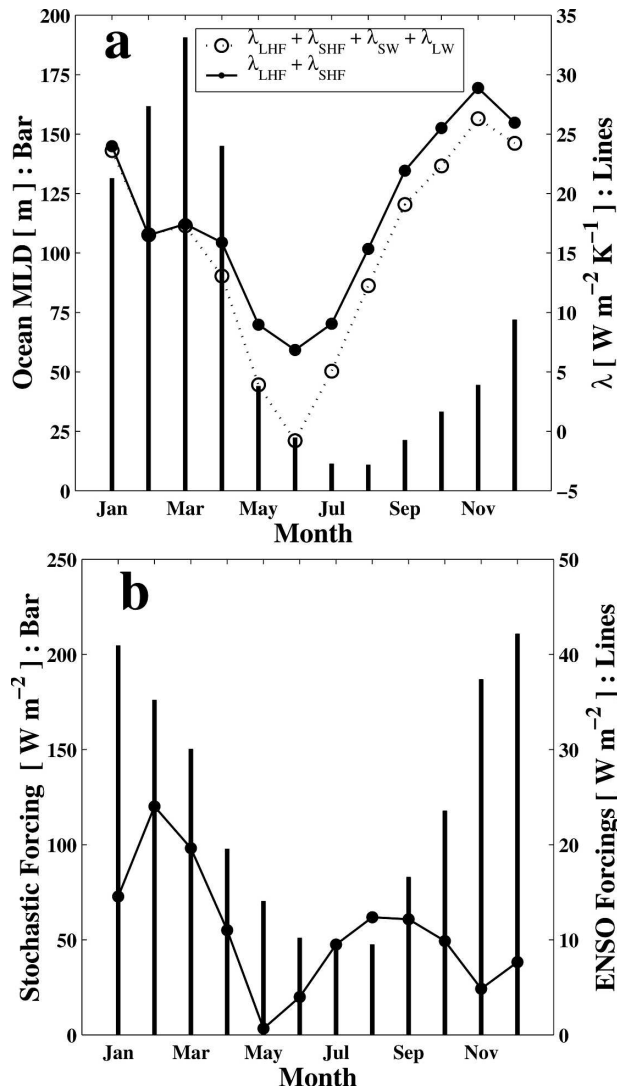


FIG. 5. (a) The observed ocean MLD (bar) and the net ($\lambda_{\text{net}} = \lambda_{\text{LHF}} + \lambda_{\text{SHF}} + \lambda_{\text{SW}} + \lambda_{\text{LW}}$; dashed line) and turbulent heat flux feedback ($\lambda_{\text{LHF}} + \lambda_{\text{SHF}}$; solid line), and (b) the magnitudes of stochastic heat flux forcing (bar) and remote heat flux ENSO forcing (lines) in the CWP region (35°–45°N, 155°–185°E). The magnitude of remote heat flux ENSO forcing is defined by $\sqrt{\sum_{i=1}^3 r_i^2}$, where r is the regression of heat flux anomalies on ENSO with local heat flux correction [see Eq. (3)] and i is the ENSO index; $\lambda_{\text{res}} = -6.5 \text{ W m}^{-2} \text{ K}^{-1}$. Note that $\lambda > 0$ indicates damping and positive radiative feedback is indicated by $\lambda_{\text{net}} < \lambda_{\text{LHF}} + \lambda_{\text{SHF}}$.

a. Control simulation and observed autocorrelations

The monthly SST autocorrelations as a function of calendar month and lag from the control simulation, which includes all feedbacks and forcings, and from observations are shown for the CWP region in Fig. 6. The simulated autocorrelations are based on the en-

semble average from a set of 50 simulations, where each ensemble member has the same ENSO forcing for the years 1951–2002, but different stochastic forcings. For a more robust estimate, the observed SST autocorrelations are based on the average of the following four different sources: the Comprehensive Ocean–Atmosphere Data Set (COADS; Woodruff et al. 1987) for 1956–97, Met Office historical SST dataset (Folland and Parker 1995) for 1950–99, Lamont-Doherty Earth Observatory analysis (Kaplan et al. 1998) for 1953–2002, and Reynolds Reconstructed SST (Reynolds and Smith 1994) for 1950–99.

Overall, the structures of the observed and simulated autocorrelations are very similar; the pattern correlation between Figs. 6a and 6b is close to 0.9 (Table 1). For the initial or reference months of January–June, the correlations in Figs. 6a and 6b decrease until fall, then increase, reaching a maximum in February–March, and then decrease again to a minimum in the following September–October. This late-winter peak in autocorrelations is the signature of the reemergence mechanism.

The high pattern correlation between observations and the model is partly due to the initial persistence of SST anomalies resulting from the thermal inertia of the upper ocean described by Frankignoul and Hasselmann (1977). To remove this basic persistence, we first fit an exponential function [$\exp(-\lambda_c \tau)$; where λ_c is a seasonal constant and τ the lag] to the SST autocorrelations for each calendar month using lags of < 5 months in both the model and observations. The observed–simulated pattern correlation is 0.66 when the exponential based on observations is subtracted from both the observations and the model, and is 0.49 when the observed and modeled exponentials are subtracted from their respective autocorrelations (Table 1). This degradation occurs because the initial persistence is too strong over the first few months of the model simulation during winter (see Figs. 6c and 6d).

Lag autocorrelations beginning in April and September and extending over the next 24 months (extended horizontal cross sections through Figs. 6a,b) are presented in Figs. 6c and 6d, respectively. Error bars given by the standard deviation of the autocorrelations obtained from the 50-member ensemble and from the four observation datasets are also shown at each lag. The model is generally consistent with the observed autocorrelation values considering the uncertainties in both estimates, except it underestimates the initial decay of the SST anomalies and does not reproduce the enhanced correlations at lags of 13–20 months for the reference month of September.

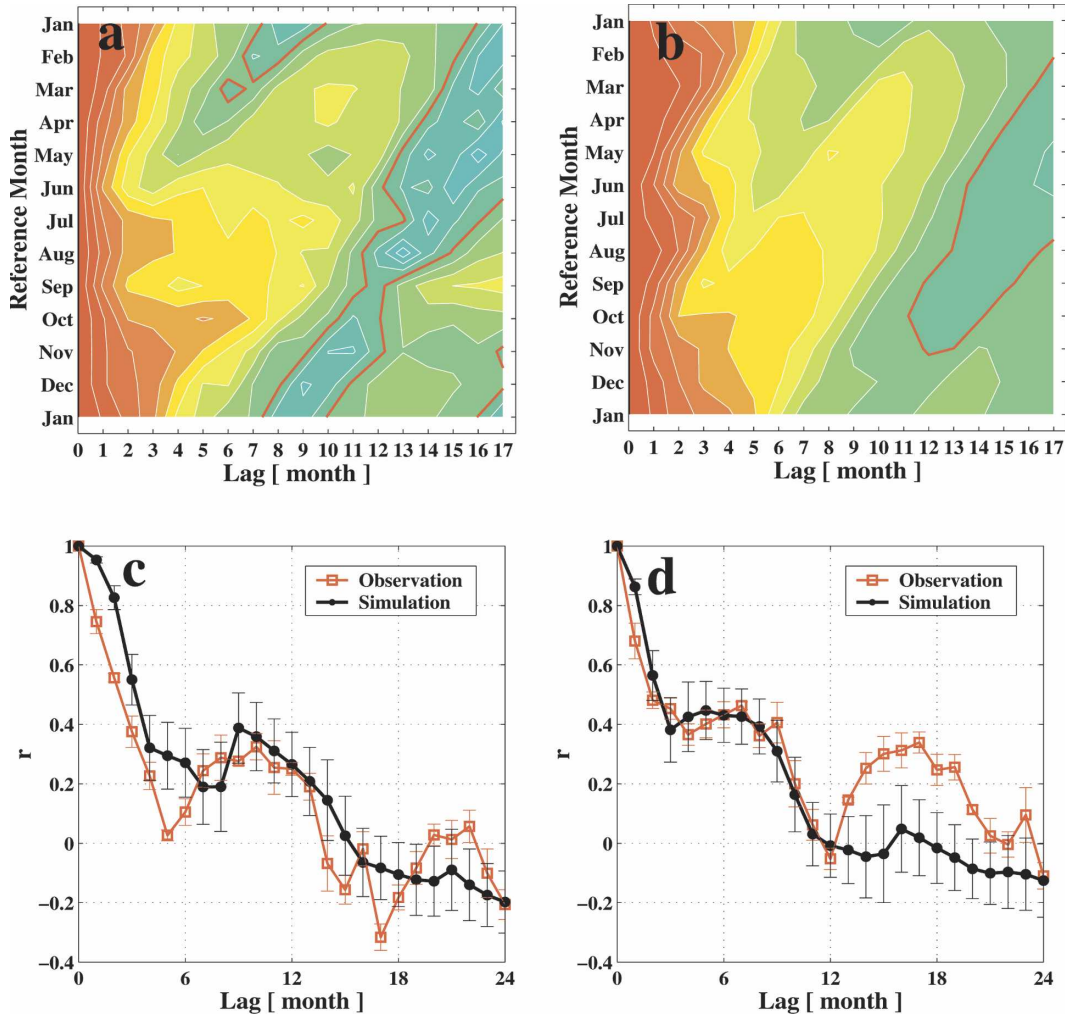


FIG. 6. Ensemble mean autocorrelation (r) of high-pass-filtered (<12.5 yr) monthly SST anomalies in CWP as a function of calendar month and lag from (a) observations obtained from the average of four different datasets and (b) 50-member ensemble of the complete stochastic model. The contour/shading interval is 0.1 and the zero contour is indicated by a red line. Lagged autocorrelations out to 24 months for the reference months of (c) April and (d) September, where vertical bars indicate one std dev of the autocorrelations at each lag.

b. Sensitivity of SST persistence to forcing and feedbacks

We assess the relative contribution of radiative feedback, remote ENSO forcing, and entrainment on the persistence of monthly SST anomalies by comparing the control simulation to a series of sensitivity simulations where one of the processes is excluded but all other model parameters and forcings are the same as in the control. The autocorrelations of monthly SST anomalies from the three sensitivity simulations are indicated as color shading in Figs. 7a–c, while the anomalous autocorrelation (Δr) values, obtained from the control minus the respective sensitivity simulation, are indicated by black lines.

The radiative feedback generally enhances SST autocorrelations in CWP for all months and lags with a maximum increase of $\Delta r \sim 0.15$ for lags terminating in August (2–6-month lags for the reference months of February–June). The change in SST persistence resulting from f'_{ENSO} has a somewhat larger amplitude ($\Delta r \sim 0.25$) but a more complex structure than that resulting from $\lambda_{\text{SW+LW}}$. ENSO forcing decreases r for lags initiated in January–July and terminating in September, but increases r for the reference months of August–October for lags of up to 10 months. An and Wang (2005) also found that ENSO enhanced the persistence of North Pacific SST anomalies in summer; although they found the maximum enhancement occurred in June–July rather than in August–September. The in-

TABLE 1. The pattern correlation between the observed and simulated autocorrelation structure of monthly SST anomalies in the three regions and in the basinwide analyses. Values are given for the full structure and with an exponential function [$\exp(-\lambda_c\tau)$] removed; the latter represents the basic decay of SST anomalies (e.g., see Frankignoul and Hasselmann 1977) and is estimated using lags of <5 months. The observed $\exp(-\lambda_c\tau)$ is always subtracted from the observed autocorrelation structure, while the observed or simulated $\exp(-\lambda_c\tau)$ is subtracted from the model's structure.

Domain	Full	Removed obs $\exp(-\lambda_c\tau)$	Removed obs and model $\exp(-\lambda_c\tau)$
CWP	0.87	0.66	0.49
CEP	0.88	0.43	0.37
SEP	0.90	0.40	0.35
Basin	0.89	0.60	0.48

crease in persistence does not necessarily imply a corresponding increase in SST variability: ENSO forcing as well as radiative feedback enhances the interannual variance of SST anomalies for all months (not shown).

The sensitivity of the SST persistence to the atmospheric bridge will likely depend on the temporal evolution of the remote ENSO forcing. Autocorrelations of f'_{ENSO} in the CWP region are shown in Fig. 8. Beginning in summer, the persistence of the remote ENSO forcing is very strong, with correlations >0.4 for lags of up to 8 months. The persistence gradually decreases through fall and winter until it reaches a minimum in May, when $r \sim 0.1$ at 1-month lag. While the short-term (<6 month) persistence is weak in spring, f'_{ENSO} exhibits strong negative correlations at lags of ~ 14 – 16 months. This is consistent with the evolution of ENSO itself, which exhibits a spring persistence barrier and some tendency for ENSO to change states over 1–2 yr (e.g., Torrence and Webster 1998). Comparison of Fig. 8 with Fig. 7b indicates that the persistence of f'_{ENSO} and SST anomalies are related to each other, with the SST autocorrelation lagging the ENSO forcing by 2–3 months. The main exception occurs for the reference months of May–June when the ENSO forcing is very weak (see Fig. 5b).

The impact of entrainment on enhancing SST persistence is relatively strong with a maximum amplitude of $\Delta r \sim 0.25$ (Fig. 7c). The largest positive anomalies occur during the lagged month of March when the ocean MLD is deepest, and thus the full extent of the thermal anomalies created during the previous winter and spring can be entrained into the mixed layer via the reemergence mechanism. Entrainment also damps SST anomalies. While entrainment reduces the initial SST persistence for nearly all reference months, it is especially pronounced for the lagged months of July–

August ($\Delta r \sim 0.45$). For the reference months of September–February, the concurrent SST and T_b anomalies are uncorrelated with each other and thus entrainment dilutes thermal anomalies in the mixed layer and thus damps SST anomalies [Eq. (1); Frankignoul 1985]. Entrainment also decreases autocorrelations of April–June SST anomalies at lags of 1–4 months, even though the mixed layer shoals and thus the entrainment forcing is zero by construction in the model. This is due to a significant decrease in the interannual variance of monthly SST anomalies by entrainment (not shown); for the same random atmospheric and ENSO forcing, autocorrelation of SST anomalies spread over a narrow range decay more rapidly than anomalies spread over a wide range.

4. The central eastern Pacific and subtropical eastern Pacific

In this section, we apply the stochastic model to regions in the central eastern Pacific (CEP; 30° – 40°N , 170° – 145°W , see Fig. 3a) and subtropical eastern Pacific (SEP; 25° – 35°N , 140° – 120°W). We chose these two regions because CEP is strongly influenced by ENSO during winter (Fig. 3a), while SEP is characterized by strong, positive radiative feedback during late summer and autumn when the MSC fraction reaches a maximum (Klein and Hartmann 1993). The MLD, feedback parameter, and forcing values are shown for the CEP (SEP) on the left (right) side of Fig. 9. Compared to the CWP region, CEP has a reduced annual cycle of MLD and stochastic forcing, stronger positive radiative feedback during late spring and early summer, and stronger (weaker) ENSO forcing during winter (summer). Relative to the other two regions, SEP has a weaker annual cycle of MLD and stochastic forcing, negligible ENSO forcing, and stronger (weaker) positive radiative feedback during August–October (March–June).

The autocorrelations for observations (top row) and for simulations without radiative feedback (second row), remote ENSO forcing (third row), and entrainment (fourth row) in the CEP (left) and SEP regions (right) are shown in Figs. 10a–h. The pattern correlation between the observed and simulated autocorrelations in CEP and SEP is ~ 0.9 , which decreases to ~ 0.4 when $\exp(-\lambda_c\tau)$ is subtracted from the original autocorrelations (Table 1). Similar to the CWP, simulations tend to overestimate the initial persistence of the SST anomalies and underestimate reemergence signals. These are speculated to be associated in part with the replacement of unresolved error sources by positive residual feedback parameters here. Positive radiative feedback has a greater impact on SST persistence in

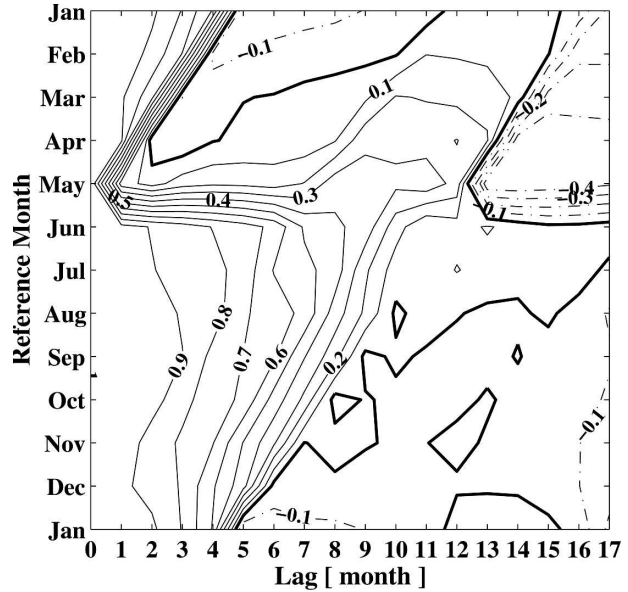
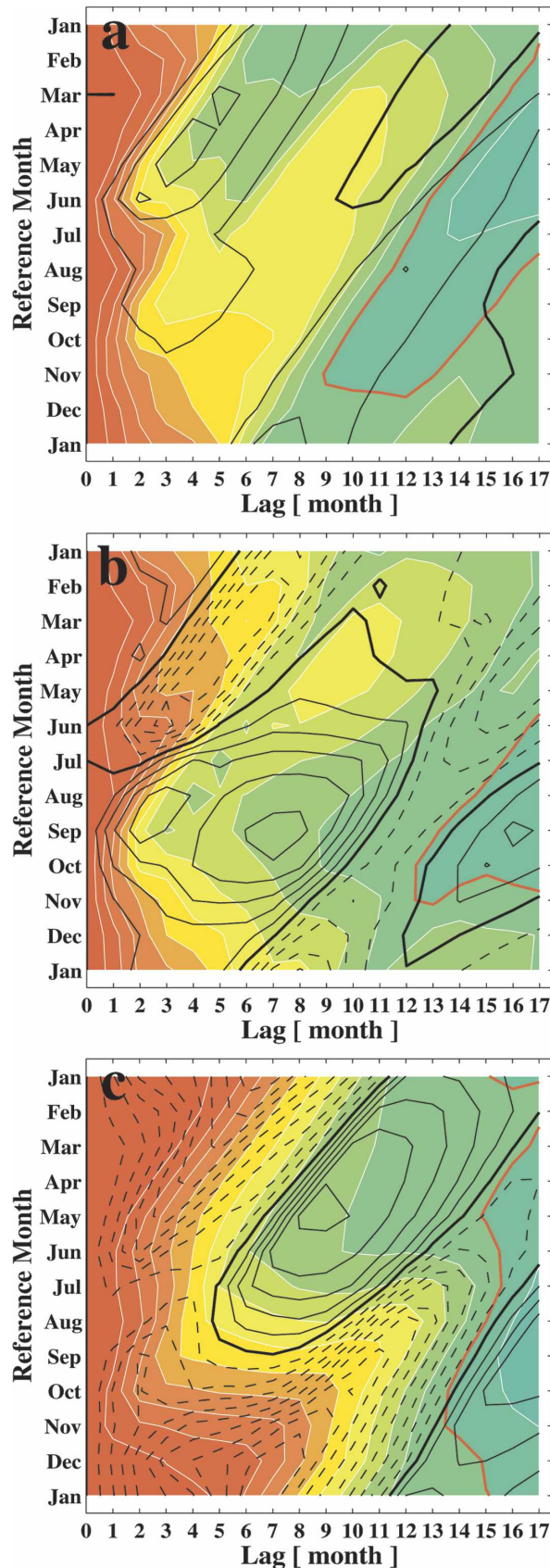


FIG. 8. Autocorrelation structure of the monthly forcing resulting from ENSO in the CWP region.

CEP (Fig. 10c) than in CWP (Fig. 7a) during spring and summer; that is, Δr has a maximum value of ~ 0.3 for lags that terminate in August, which is roughly double the corresponding CWP value. Another positive anomaly center in Fig. 10c occurs at a lag of 4 months for the reference month of August ($\Delta r \sim 0.2$). The radiative feedback is largest in fall to early winter in SEP, although its impact on SSTs is modest (Fig. 10d; $\Delta r \sim 0.1$). In general, f'_{ENSO} decreases (increases) SST persistence for the reference months of February–June (July–December) for lags of up to 1 yr. In contrast, f'_{ENSO} has a negligible impact on the SST persistence in SEP. The general pattern of Δr resulting from entrainment in CEP and SEP are similar to the pattern in CWP, but systematic differences exist in the timing and strength of the reemergence mechanism.

5. Basinwide analysis

a. Stochastic model

In this section, we examine the persistence of the dominant mode of monthly SST anomalies in the North

FIG. 7. The total (shading; interval 0.1) and anomalous ($\Delta r =$ control simulation – sensitivity simulation, black contours; interval 0.05) autocorrelations of the sensitivity simulations without (a) radiative feedback, (b) remote ENSO forcing, and (c) entrainment in the CWP region. Red lines indicate zero autocorrelation. All analyses are based on high-pass-filtered (<12.5 yr) monthly SST anomalies.

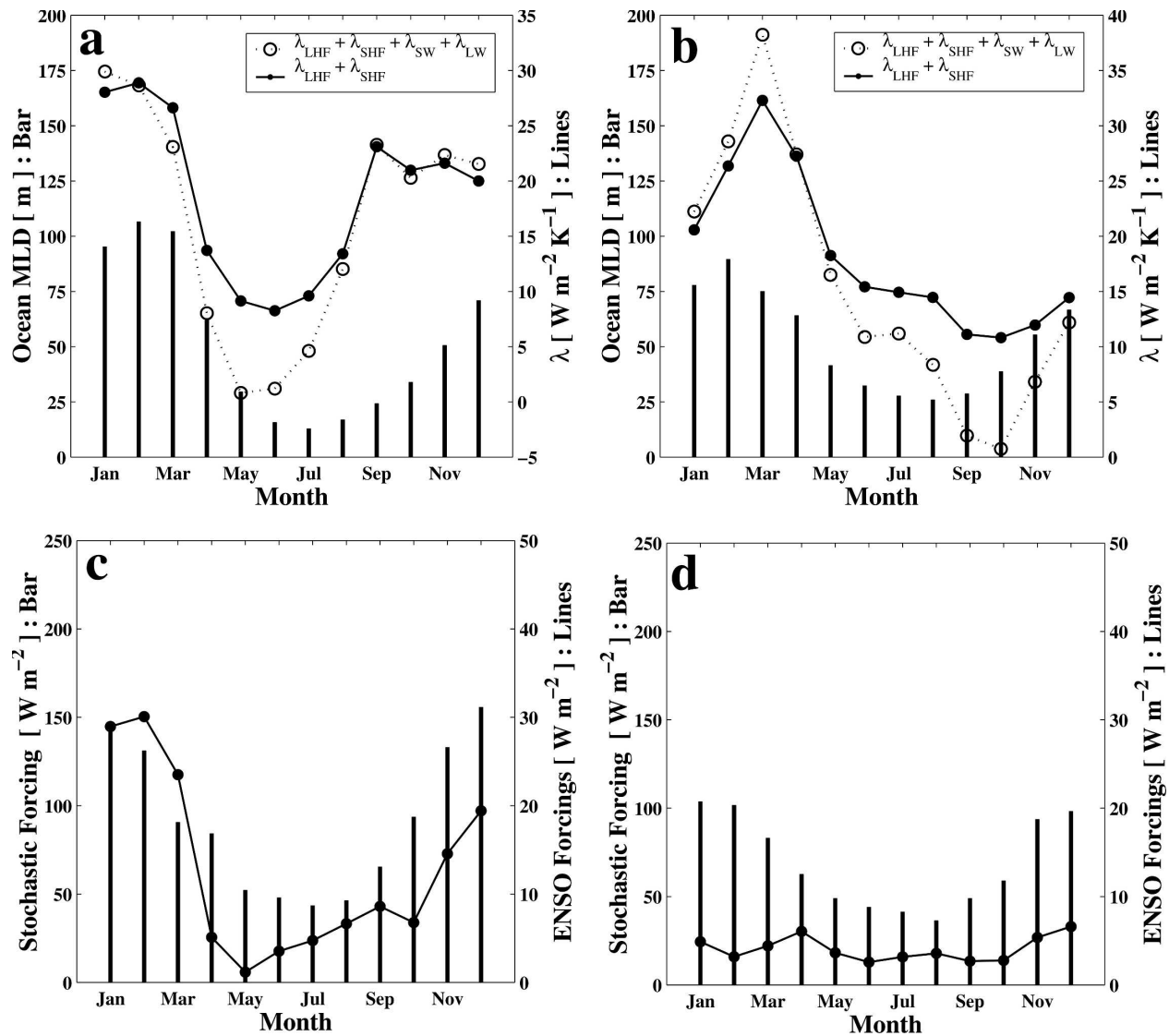


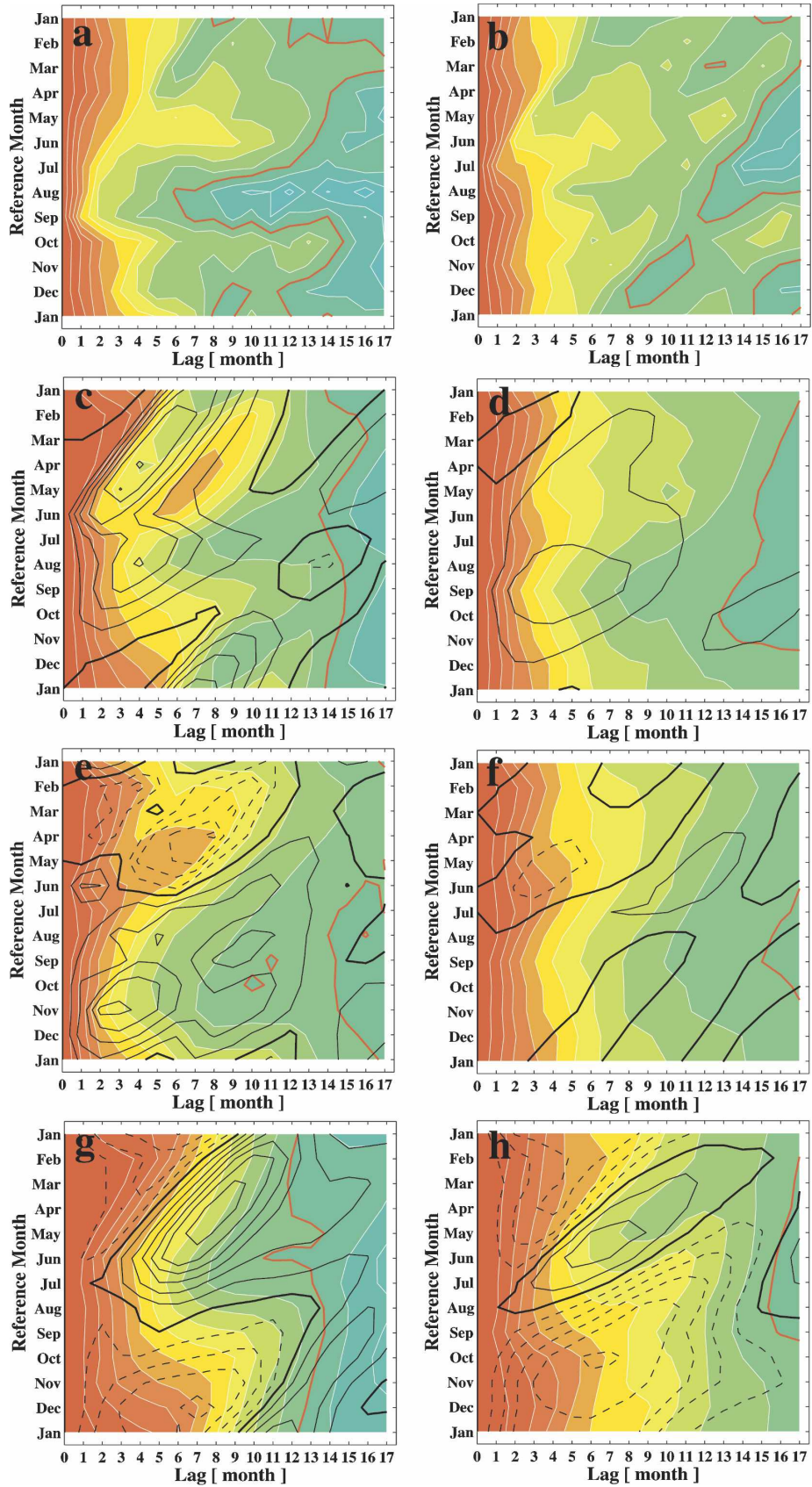
FIG. 9. As in Fig. 5, but for the (left) CEP (30°–40°N, 170°–145°W) and (right) SEP (25°–35°N, 140°–120°W) regions. (a), (b) The observed MLD (bars) and heat flux feedback parameters (lines), and (c), (d) the magnitude of stochastic heat flux forcing (bars) and the remote heat flux ENSO forcing (lines) are shown; $\lambda_{res} = -3.1 \text{ W m}^{-2} \text{ K}^{-1}$ in the CEP and $\lambda_{res} = -6.5 \text{ W m}^{-2} \text{ K}^{-1}$ in the SEP.

Pacific Ocean. A 50-member ensemble of the control and the three sensitivity simulations were performed using the ENSO and stochastic forcing (described in section 2) for all North Pacific grid squares during the years 1951–2002. EOF analyses were performed on the simulated monthly SST anomalies on the 5° latitude \times 5° longitude grid and compared with observations. The

observed SST autocorrelations shown here are based on the projections of the four different sources of monthly SST anomalies (see section 3a) on the observed dominant mode obtained from Reynolds and Smith (1994) over a 50-yr period (1950–99).

The observed and simulated dominant patterns of monthly SST anomalies are shown in Fig. 11. In gen-

FIG. 10. Same as Fig. 7, but the total (shaded) and anomalous (contours) autocorrelations in the (left) CEP and (right) SEP regions, with the observed autocorrelations in the top panels. All analyses are based on high-pass-filtered (<12.5 yr) monthly SST anomalies in the CEP and SEP regions.



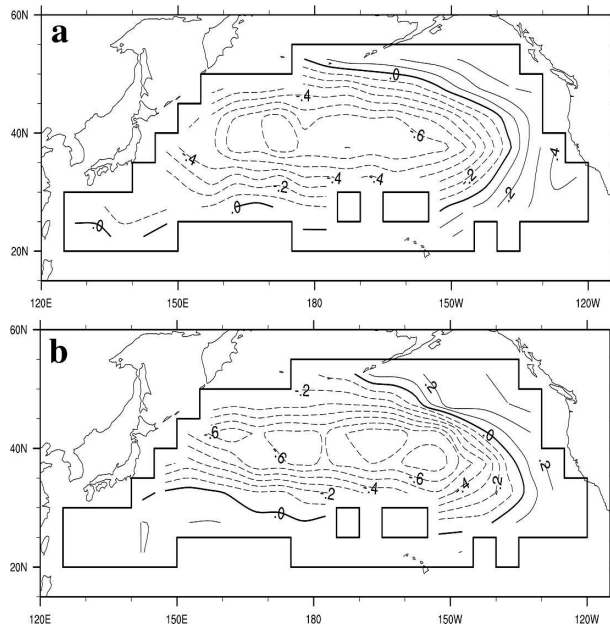


FIG. 11. The (a) observed and (b) simulated dominant pattern of the total (unfiltered) monthly SST anomalies over the North Pacific. Contour interval is 0.1 K with solid (dotted) lines for positive (negative) anomalies. The observations were obtained from Reynolds and Smith (1994) for a 50-yr period (1950–99), while the simulated results are based on a 50-member ensemble for a 52-yr period (nominally 1951–2002). The fraction of variance explained by EOF 1 is 28.8% (22.2%) for observations (the model). The pattern correlation between (a) and (b) is 0.90.

eral, the simulation reproduces the observed leading EOF structure (a pattern correlation of 0.9) with similar fractions of variance explained by the leading EOFs (28.8% for the observation, 22.2% for the simulation).

The autocorrelations of the observed and simulated monthly SST anomalies projected on the *observed* dominant mode are shown in Figs. 12a and 12b, respectively. (The autocorrelation pattern of the simulated dominant PC is similar to Fig. 12b; not shown.) The simulated autocorrelation pattern of the dominant mode, which resembles the autocorrelation pattern in the CWP region (Fig. 6b), resembles observations (Table 1).

The total (shading) and anomalous (lines) autocorrelations of the simulated PC projected on the observed dominant mode for the three sensitivity experiments are shown in Fig. 13. The anomalous SST persistence patterns are similar to those in the CWP region (Fig. 7) in that Δr is (a) enhanced by positive radiative feedback centered on the lags terminating in August ($\Delta r \sim 0.2$); (b) reduced by remote ENSO forcing for lags terminating in September ($\Delta r \sim -0.25$), but enhanced in other seasons for lags of up to 1 yr ($\Delta r \sim 0.25$); and (c) strongly damped by entrainment in summer ($\Delta r \sim -0.4$) and enhanced afterward, reaching a maximum in January–February resulting from the reemergence mechanism ($\Delta r \sim 0.3$). As in the local analysis, a change in SST persistence does not necessarily mean a similar change in SST variability, that is, ENSO forcing enhances SST variability while entrainment reduces it (not shown).

b. AGCM–MLM simulations

To verify the results from the stochastic simulations, we analyzed output from an AGCM coupled to an ocean MLM, which provides a more complete repre-

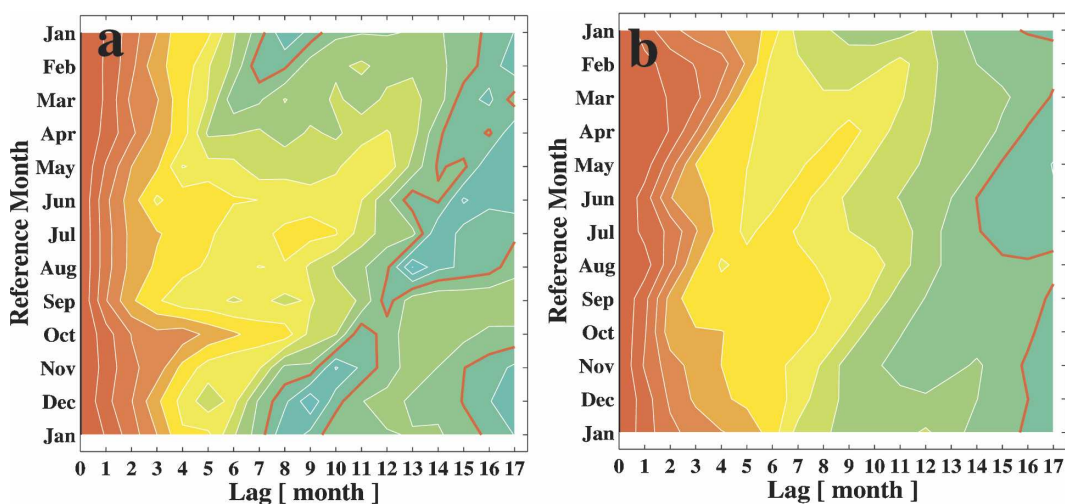
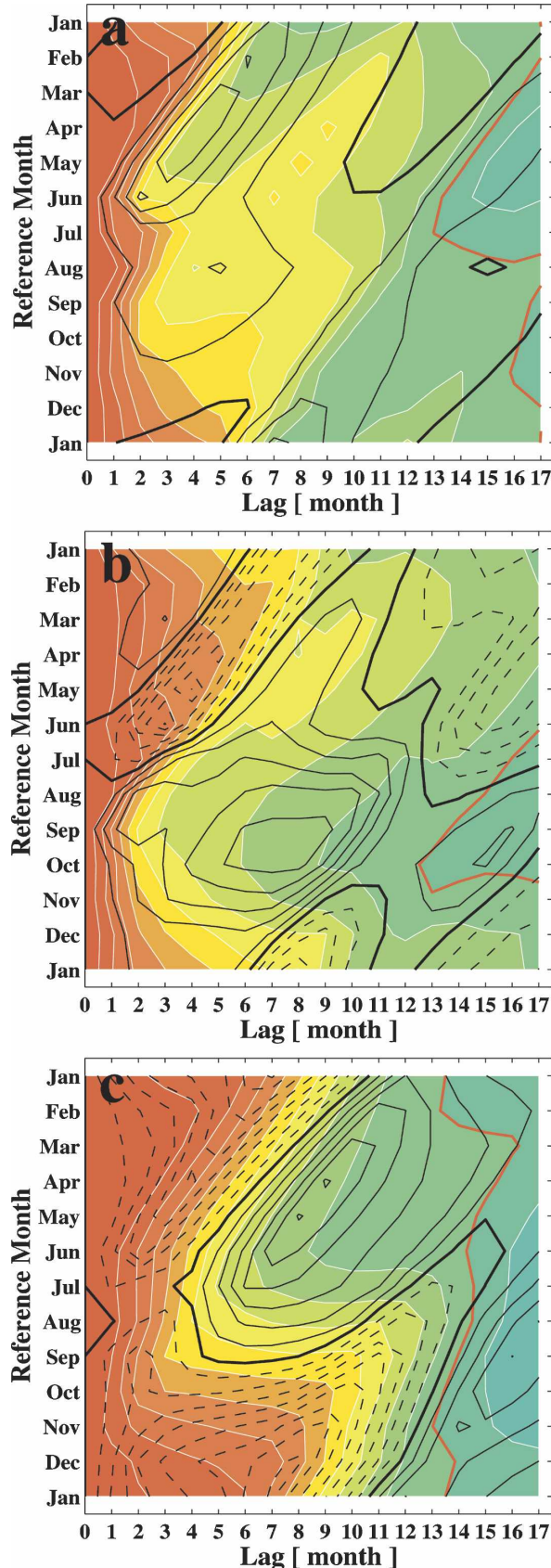


FIG. 12. Persistence of the (a) observed and (b) simulated leading first PC of North Pacific SST anomalies as a function of the reference calendar month and lag as obtained from the high-pass-filtered (<12.5 yr) time series of the projection of the (a) simulated and (b) observed monthly SST anomalies on the observed leading EOF (Fig. 11a).



sensation of the relevant physical processes, including air–sea interaction, ENSO forcing, and entrainment. We make use of an ensemble of 16 Geophysical Fluid Dynamics Laboratory (GFDL) R30 AGCM–MLM integrations, described by Alexander et al. (2002). Each simulation spans the period of 1950–99 and consists of observed monthly SSTs prescribed in the eastern tropical Pacific (15°N–15°S, 172°E–South American coast) and a grid of one-dimensional mixed layer models over the remainder of the global oceans. This model configuration incorporates ENSO variability through the boundary forcing in the tropical Pacific, which is communicated to the global oceans via the atmospheric bridge. The ocean model simulates mixed layer temperature (=SST), salinity, and depth, resulting from air–sea fluxes and entrainment. In contrast to the stochastic simulations, the mixed layer is not constrained to follow the mean seasonal cycle in the MLM, allowing for variability in MLD, W_e , and T_b to impact SST' [see Eq. (1); Alexander et al. 2000]. There are no currents, however, or any other communication between grid cells.

The leading pattern of the “total” variability in AGCM–MLM over the North Pacific (Fig. 14a) is obtained from the first EOF of monthly SST variability where all 16 simulations have been concatenated to form an 800-yr time series. The dominant pattern of the North Pacific SST variability in the AGCM–MLM is similar to both the stochastic simulation and observations; that is, the pattern correlation between Fig. 14a and Fig. 11a (Fig. 11b) is 0.89 (0.76). The fraction of variance explained by EOF 1 (17.7%), however, is smaller than in observations (28.8%). The autocorrelation structure of the first PC obtained from the total SST time series in the AGCM–MLM experiment (color shading in Fig. 14b) resembles the autocorrelations from observations and the stochastic model (Fig. 13), although the reemerging anomalies occur at shorter lags and the decay of summertime SST anomalies occurs more rapidly in the MLM compared to in nature.

The ENSO-related SST signal is estimated by first ensemble averaging the monthly anomalies, which greatly reduces the internal variability in the atmosphere–ocean system, before computing the leading EOF over the North Pacific, and the “residual” is the obtained from the SST anomalies with the ensemble

FIG. 13. Same as Fig. 7, but for the high-pass-filtered (<12.5 yr) time series of the simulated monthly SST anomalies projected on the observed leading EOF (Fig. 11a) for the sensitivity simulations without (a) radiative feedback, (b) ENSO forcing, and (c) entrainment.

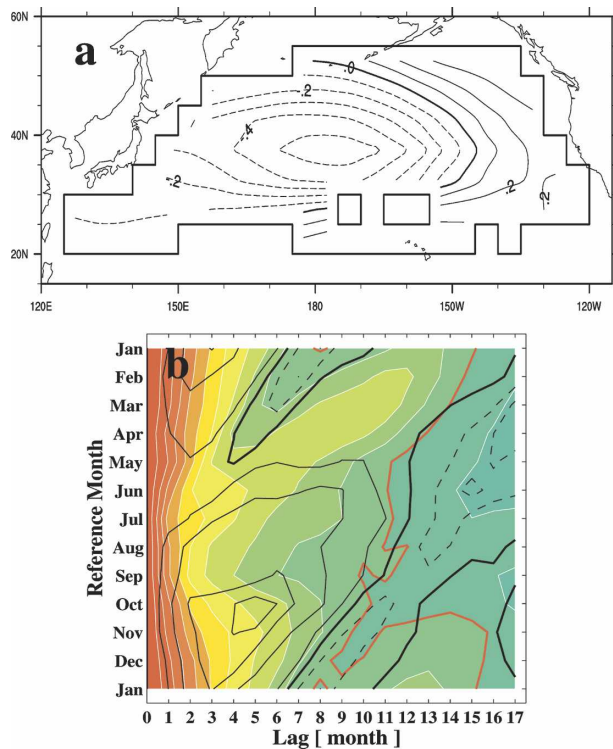


FIG. 14. Analysis of 16 50-yr simulations of an AGCM that has observed SSTs specified in the tropical Pacific for the period 1950–99 and is also coupled to a mixed layer model over the rest of the global oceans. (a) EOF 1 of the “total” unfiltered monthly SST anomalies over the North Pacific, in which all 16 simulations have been strung together to form one long time series. (b) The autocorrelations of the corresponding PC of the total variability (shading; interval 0.1) and the variability resulting from ENSO (contours; interval 0.05) obtained from the first PC of the 16-member ensemble mean. The fraction of variance explained by EOF 1 in (a) is 17.7%.

mean removed and includes the impact of air–sea interaction and entrainment on SSTs. ENSO (lines in Fig. 14b) enhances the persistence of North Pacific SST anomalies, especially from late summer through the following winter, as in the stochastic simulation (Fig. 13b). The close correspondence between Δr obtained from the stochastic model and the AGCM–MLM is indicated by the high pattern correlation (0.75) and low mean absolute difference (0.06) between the two.

6. Summary and discussion

We investigated how cloud radiative feedback, remote ENSO forcing, and oceanic entrainment contribute to the persistence of monthly SST anomalies in the North Pacific using a stochastically forced ocean mixed layer model. The radiative feedback and ENSO forcing were directly estimated from observations, while the

stochastic forcing was derived from an AGCM simulation with climatological SSTs as boundary conditions: all three forcings are a function of month and location. The heat flux through the base of the mixed layer depends on the entrainment rate and temperature anomalies within and below the mixed layer. The entrainment rate, obtained from the observed climatological ocean MLD, repeats the same annual cycle each year. The anomalous temperature at a given level within the seasonal thermocline is initially set to the SST anomaly when the MLD shoals to that level in spring. It is subsequently reduced by weak, linear damping and then is reentrained into the surface layer when the MLD deepens to that level in the following fall or winter. Finally, neglected physical processes and model biases are crudely represented in the model by specifying a constant residual feedback parameter that forces the simulated SST variance to match the observed variance in each $5^\circ \times 5^\circ$ grid square. The contribution of the radiative feedback, ENSO forcing, and entrainment on the high-pass-filtered (<12.5 yr) SST autocorrelations is examined by comparing simulations without each process to the full or control simulation.

The model simulates the observed SST autocorrelation structure in the central western Pacific (CWP) region reasonably well. Radiative feedback enhances the persistence of winter–spring SST anomalies for lags ending in August. ENSO-induced forcing tends to reduce the persistence of winter–spring SST anomalies for lags terminating in September, but it enhances autocorrelations for the reference period of August–October especially for lags of 2–9 months. The sensitivity of SSTs to ENSO forcing depends on the persistence of that forcing. Entrainment reduces SST persistence for lags ending in July–August and enhances it for lags extending to March. The latter reflects the reemergence of SST anomalies that were stored below the mixed layer in summer, while the former is a combined result of entrainment diluting the SST anomalies initiated in fall and winter and suppressing SST variability throughout the year.

Similar analyses were performed in the central eastern Pacific (CEP) and subtropical eastern Pacific (SEP) regions. In CEP, radiative enhancement of SST persistence is generally similar to but stronger than that in CWP, while in SEP the maximum radiative enhancement occurs during August–October at lags of 3–6 months. Remote ENSO forcing can either enhance or reduce SST persistence in the CEP, while it has a negligible impact on persistence in the SEP. The enhancement of SST persistence by the reemergence mechanism is weakest in SEP, while damping is strongest

(weakest) in the CWP (CEP) due partly to the strong (weak) suppression of SST variability by entrainment.

Finally, we examined the persistence of the dominant pattern of SST variability across the North Pacific. The impact of radiative feedback, ENSO, and entrainment on SST persistence are generally similar to those in the CWP, because the maximum loading of the leading EOF of SST is centered in this region. The winter-to-spring persistence of the dominant mode is slightly enhanced by remote ENSO forcing but is reduced by entrainment with a negligible contribution by radiative feedback. However, late-spring-to-summer persistence is strongly enhanced by radiative feedback but reduced by entrainment by a comparable amount. Zhang et al. (1998) found that in spite of shallow MLD in summer, the summer-to-winter persistence of the dominant mode of North Pacific SST anomalies is stronger than winter-to-summer persistence, which they attributed to strong, positive radiative feedback during summer in association with marine stratiform clouds (Norris et al. 1998). While our results show that radiative feedback enhances summer-to-winter SST persistence, as hypothesized by Zhang et al. (1998) and Norris et al. (1998), this effect is modest ($\Delta r < 0.1$), and entrainment and remote ENSO forcing have a greater impact on the summer-to-winter persistence ($\Delta r \sim 0.15\text{--}0.2$) than the radiative feedback. However, it should be noted that the impact of these processes might not be isolated from each other. For example, ENSO can create SST anomalies during both winter and summer—the former can be stored beneath the mixed layer in summer and recur in the following winter, while the latter can be enhanced by positive MSC–SST feedback.

We also examined the autocorrelation structure of the dominant mode of North Pacific SST anomalies obtained from a AGCM coupled to a variable-depth mixed layer ocean model forced by observed SSTs in the tropical Pacific. The full autocorrelation structure and the influence of ENSO forcing on this structure were similar to the stochastic simulations and nature. This suggests that both types of models can provide insight into how various processes influence the evolution of extratropical SST anomalies.

Several processes not included in the entraining mixed layer model may also influence extratropical SST persistence. In addition to its impact on surface fluxes on monthly time scales, ENSO also affects the strength and location of the North Pacific storm track (e.g., Renwick and Wallace 1996; Compo et al. 2001), and thus will modulate the stochastic forcing—a process that is not included here. In addition, entrainment is treated in a highly idealized manner and does not include sub-monthly or interannual fluctuations in the entrainment

rate or how processes such as subduction, Rossby waves, or Ekman pumping influence the temperature anomalies in the seasonal thermocline (e.g., Schneider and Miller 2001). For example, subduction and mixing within the seasonal thermocline can remove anomalies before they can return to the surface layer in the subsequent winter, while ocean currents can advect temperature anomalies downstream so that winter SST anomalies reemerge at another location (de Coëtlogon and Frankignoul 2003; Sugimoto and Hanawa 2005a,b). Also, it is likely that fluctuations in ocean heat transport have a significant impact on SST persistence in portions of the North Pacific, such as the Kuroshio region (Qiu 2002). Investigation of the impact of these additional oceanic processes upon SST anomaly persistence in the North Pacific, particularly on time scales longer than a decade, is left to future work.

Acknowledgments. We thank Dr. R. Saravanan for providing the atmospheric heat fluxes from CAM3 and for his helpful comments. Dr. G. P. Compo provided helpful advice on statistical analysis. We also thank the editor and three anonymous reviewers for constructive comments. The Reynolds Reconstructed data were obtained from the NOAA–CIRES Climate Diagnostics Center Web site (online at <http://www.cdc.noaa.gov>). Sungsu Park was supported by the Advanced Study Program. Clara Deser and Michael Alexander gratefully acknowledge support from NOAA Office of Global Programs CLIVAR Project.

REFERENCES

- Alexander, M. A., 1992: Midlatitude atmosphere–ocean interaction during El Niño. Part I: The North Pacific Ocean. *J. Climate*, **5**, 944–958.
- , and C. Deser, 1995: A mechanism for the recurrence of wintertime midlatitude SST anomalies. *J. Phys. Oceanogr.*, **25**, 122–137.
- , and C. Penland, 1996: Variability in a mixed layer ocean model driven by stochastic atmospheric forcing. *J. Climate*, **9**, 2424–2442.
- , C. Deser, and M. S. Timlin, 1999: The reemergence of SST anomalies in the North Pacific Ocean. *J. Climate*, **12**, 2419–2433.
- , J. D. Scott, and C. Deser, 2000: Processes that influence sea surface temperature and ocean mixed layer depth variability in a coupled model. *J. Geophys. Res.*, **105**, 16 823–16 842.
- , I. Blade, M. Newman, J. R. Lanzante, N. C. Lau, and J. D. Scott, 2002: The atmospheric bridge: The influence of ENSO teleconnections on air–sea interaction over the global oceans. *J. Climate*, **15**, 2205–2231.
- , N. C. Lau, and J. D. Scott, 2004: Broadening the atmospheric bridge paradigm: ENSO teleconnection to the tropical West Pacific–Indian Oceans over the seasonal cycle and to the North Pacific in summer. *Earth's Climate: The Ocean–*

- Atmosphere Interaction, Geophys. Monogr.*, Amer. Geophys. Union, Vol. 147, 85–104.
- An, S.-I., and B. Wang, 2005: The forced and intrinsic low-frequency modes in the North Pacific. *J. Climate*, **18**, 876–885.
- Barlow, M., S. Nigam, and E. H. Berbery, 2001: ENSO, Pacific decadal variability, and U.S. summertime precipitation, drought, and streamflow. *J. Climate*, **14**, 2105–2128.
- Bretherton, C. S., and M. C. Wyant, 1997: Moisture transport, lower-tropospheric stability, and decoupling of cloud-topped boundary layers. *J. Atmos. Sci.*, **54**, 148–167.
- Cayan, D. R., 1992: Latent and sensible heat flux anomalies over the Northern Oceans: Driving the sea surface temperature. *J. Phys. Oceanogr.*, **22**, 859–881.
- Compo, G. P., P. D. Sardeshmukh, and C. Penland, 2001: Changes of subseasonal variability associated with El Niño. *J. Climate*, **14**, 3356–3374.
- de Coëtlogon, G., and C. Frankignoul, 2003: The persistence of winter sea surface temperature in the North Atlantic. *J. Climate*, **16**, 1364–1377.
- Deser, C., M. A. Alexander, and M. S. Timlin, 2003: Understanding the persistence of sea surface temperature anomalies in midlatitudes. *J. Climate*, **16**, 57–72.
- , A. S. Phillips, and J. W. Hurrell, 2004: Pacific interdecadal climate variability: Linkages between the Tropics and the North Pacific during boreal winter since 1900. *J. Climate*, **17**, 3109–3124.
- Folland, C. K., and D. E. Parker, 1995: Correction of instrumental biases in historical sea surface temperature data. *Quart. J. Roy. Meteor. Soc.*, **121**, 319–367.
- Frankignoul, C., 1985: Sea surface temperature anomalies, planetary waves and air-sea feedback in the middle latitudes. *Rev. Geophys.*, **23**, 357–390.
- , and K. Hasselmann, 1977: Stochastic climate models. Part 2. Application to sea-surface temperature variability and thermocline variability. *Tellus*, **29**, 289–305.
- , and R. W. Reynolds, 1983: Testing a dynamical model for mid-latitude sea surface temperature anomalies. *J. Phys. Oceanogr.*, **13**, 1131–1145.
- Herterich, K., and K. Hasselmann, 1987: Extraction of mixed layer advection velocities, diffusion coefficients, feedback factors and atmospheric forcing parameters from the statistical analysis of North Pacific SST anomaly fields. *J. Phys. Oceanogr.*, **17**, 2145–2156.
- Hoskins, B. J., 1996: On the existence and strength of the summer subtropical anticyclone. *Bull. Amer. Meteor. Soc.*, **77**, 1287–1292.
- Kaplan, A., M. A. Cane, Y. Kushnir, A. C. Clement, M. B. Blumenthal, and B. Rajagopalan, 1998: Analyses of global sea surface temperature 1856–1991. *J. Geophys. Res.*, **103**, 18 567–18 590.
- Klein, S. A., and D. L. Hartmann, 1993: The seasonal cycle of low stratiform clouds. *J. Climate*, **6**, 1587–1606.
- , —, and J. R. Norris, 1995: On the relationships among low-cloud structure, sea surface temperature, and atmospheric circulation in the summertime northeast Pacific. *J. Climate*, **8**, 1140–1155.
- Lau, N. C., and M. J. Nath, 1996: The role of the “atmospheric bridge” in linking tropical Pacific ENSO events to extratropical SST anomalies. *J. Climate*, **9**, 2036–2057.
- Monterey, G. I., and S. Levitus, 1997: *Climatological Cycle of Mixed Layer Depth in the World Ocean*. U.S. Gov. Printing Office, NOAA NESDIS, 5 pp. + 87 figs.
- Namias, J., and R. M. Born, 1970: Temporal coherence in North Pacific sea-surface temperature patterns. *J. Geophys. Res.*, **75**, 5952–5955.
- , and —, 1974: Further studies of temporal coherence in North Pacific sea surface temperatures. *J. Geophys. Res.*, **79**, 797–798.
- , X. Yuan, and D. R. Cayan, 1988: Persistence of North Pacific sea surface temperature and atmospheric flow patterns. *J. Climate*, **1**, 682–703.
- Norris, J. R., 2000: Interannual and interdecadal variability in the storm track, cloudiness, and sea surface temperature over the summertime North Pacific. *J. Climate*, **13**, 422–430.
- , and C. B. Leovy, 1994: Interannual variability in stratiform cloudiness and sea surface temperature. *J. Climate*, **7**, 1915–1925.
- , Y. Zhang, and J. M. Wallace, 1998: Role of low clouds in summertime atmosphere-ocean interactions over the North Pacific. *J. Climate*, **11**, 2482–2490.
- North, G. R., T. L. Bell, R. F. Cahalan, and F. J. Moeng, 1982: Sampling errors in the estimation of empirical orthogonal functions. *Mon. Wea. Rev.*, **110**, 699–706.
- Ostrovskii, A., and L. Piterbarg, 1995: Inversion for heat anomaly transport from sea surface temperature time series in the northwest Pacific. *J. Geophys. Res.*, **100**, 4845–4865.
- , and —, 2000: Inversion of upper ocean temperature time series for entrainment, advection, and diffusivity. *J. Phys. Oceanogr.*, **30**, 201–214.
- Park, S., 2004: Remote ENSO influence on Mediterranean sky conditions during late summer and autumn: Evidence for a slowly evolving atmospheric bridge. *Quart. J. Roy. Meteor. Soc.*, **130**, 2409–2422.
- , and C. B. Leovy, 2004: Marine low cloud anomalies associated with ENSO. *J. Climate*, **17**, 3448–3469.
- , —, and M. A. Rozendaal, 2004: A new heuristic Lagrangian marine boundary layer cloud model. *J. Atmos. Sci.*, **61**, 3002–3024.
- , C. Deser, and M. A. Alexander, 2005: Estimation of the surface heat flux response to sea surface temperature anomalies over the global oceans. *J. Climate*, **18**, 4582–4599.
- Qiu, B., 2002: The Kuroshio Extension system: Its large-scale variability and role in the midlatitude ocean-atmosphere interaction. *Japan J. Oceanogr.*, **58**, 57–75.
- Renwick, J. A., and J. M. Wallace, 1996: Relationships between North Pacific wintertime blocking, El Niño, and the PNA pattern. *Mon. Wea. Rev.*, **124**, 2071–2076.
- Reynolds, R. W., 1978: Sea surface temperature anomalies in the North Pacific Ocean. *Tellus*, **30**, 97–103.
- , and T. M. Smith, 1994: Improved global sea surface temperature analyses using optimum interpolation. *J. Climate*, **7**, 929–948.
- Schneider, N., and A. J. Miller, 2001: Predicting western North Pacific Ocean climate. *J. Climate*, **14**, 3997–4002.
- Sugimoto, S., and K. Hanawa, 2005a: Remote reemergence areas of winter sea surface temperature anomalies in the North Pacific. *Geophys. Res. Lett.*, **32**, L01606, doi:10.1029/2004GL021410.
- , and —, 2005b: Why does reemergence of winter sea surface temperature anomalies in the North Pacific not occur in eastern mode water areas? *Geophys. Res. Lett.*, **32**, L15608, doi:10.1029/2005GL022968.
- Torrence, C., and P. J. Webster, 1998: The annual cycle of persis-

- tence in the El Niño/Southern Oscillation. *Quart. J. Roy. Meteor. Soc.*, **124**, 1985–2004.
- Trenberth, K. E., and D. P. Stepaniak, 2001: Indices of El Niño evolution. *J. Climate*, **14**, 1697–1701.
- , G. W. Branstator, D. Karoly, A. Kumar, N. C. Lau, and C. F. Ropelewski, 1998: Progress during TOGA in understanding and modeling global teleconnections associated with tropical sea surface temperatures. *J. Geophys. Res.*, **103**, 14 291–14 324.
- Wallace, J. M., and D. S. Gutzler, 1981: Teleconnections in the geopotential height fields during the Northern Hemisphere winter. *Mon. Wea. Rev.*, **109**, 784–812.
- Weare, B., 1994: Interrelationships between cloud properties and SSTs on seasonal and interannual timescales. *J. Climate*, **7**, 248–260.
- Woodruff, S. D., R. J. Slutz, R. L. Jenne, and P. M. Steurer, 1987: A Comprehensive Ocean Atmosphere Data Set. *Bull. Amer. Meteor. Soc.*, **68**, 1239–1250.
- Zhang, Y., J. R. Norris, and J. M. Wallace, 1998: Seasonality of large-scale atmosphere–ocean interaction over the North Pacific. *J. Climate*, **11**, 2473–2481.